



University of Crete  
Department of Physics

Rafail Skalidis

# **Study of the width of filamentary structures in interstellar molecular clouds**



Supervisor:

Professor Konstantinos Tassis

---

Heraklion September 2016



# Contents

<b>1</b>	<b>Introduction</b>	<b>3</b>
<b>2</b>	<b>Power Spectral Density</b>	<b>7</b>
2.1	One Dimensional Power Spectrum . . . . .	7
2.2	Two Dimensional Power Spectrum . . . . .	8
2.2.1	Properties of 2-D Power Spectrum . . . . .	8
2.2.2	Examples of 2-D Power Spectra . . . . .	10
<b>3</b>	<b>Azimuthally Averaged Power Spectrum</b>	<b>13</b>
3.1	Derivation of SPS . . . . .	13
3.1.1	From Spatial to Frequency Domain . . . . .	14
3.2	Verification of the Code . . . . .	15
3.3	SPS of Fractal Image . . . . .	15
<b>4</b>	<b>Filament Identification and Analysis of Fractal Image</b>	<b>19</b>
4.1	The Methodology . . . . .	19
4.2	Analysis Results . . . . .	20
<b>5</b>	<b>Simulations</b>	<b>22</b>
5.1	The Methodology . . . . .	23
5.1.1	Verification of the Code . . . . .	23
5.2	Analysis . . . . .	24
5.3	Analysis Results . . . . .	29
<b>6</b>	<b>Conclusion</b>	<b>31</b>

# Acknowledgments

I would like to express the deepest appreciation to my supervisor K.Tassis, who continually and convincingly conveyed a spirit of creativity in regard to the work. Many thanks to G.V.Panopoulou and I. Psaradaki, who provided me with the DisPerSe and FILTER analysis, the fractal image, and the technical support. Finally, I would like to express my gratitude to Dr K.Xristidis for fruitful discussions and his constant moral.

# Chapter 1

## Introduction

In the Galaxy there are billions of stars. As far as we know the space between these stars contains gasses, mostly hydrogen and helium, dust grains and cosmic rays. All the above are what we call *Interstellar Medium (ISM)*. In ISM, there are some high density regions referred as *Atomic Hydrogen Clouds* and *Interstellar Molecular Clouds*, depending on the dominant material they consist of. *Molecular Clouds* is where new stars are born in.

The earliest phases of star formation are not yet well understood, hence a lot of observations have been made, in order to find out the basic properties of the clouds. *Herschel* Space Observatory provided images of high resolution, which they reveal that in every interstellar cloud a filamentary network exists. As it is defined [André et al., 2010, Molinari et al., 2010] *filament* is an over density cylindrical structure with aspect ratio length to width of 5-10. In Fig.1.1, the right panel shows what is traced as filamentary network in cloud Polaris Flare [André et al., 2010]. These structures are very important for the star formation process, because it is believed that they are the structures that form first and then protostars appear.

A lot of effort has been exerted to understand the physical properties of filaments. The dominant theory supports that they are formed due to compressed gas caused by supersonic turbulence [Padoan et al., 2001, Porter et al., 1994, Vázquez-Semadeni, 1994]. Various sources of supersonic turbulence exist in the ISM out of which molecular clouds, and so filamentary networks, can arise like supernovae, galactic spiral shocks, expanding HII regions. Various models have been proposed involving gravitational instabilities as the formation mechanism of molecular clouds. A basic property, found by Arzoumanian et al. [2011] is that, filaments have a characteristic width

(radius) approximately 0.1 pc, as illustrated in Fig.1.2 They studied eight different regions, 278 filaments overall and concluded that the distribution of filaments' mean width values, peaks at 0.1 pc. Different interpretations have been given to explain this result. One of them supports that, the filament width is comparable to the cutoff of MHD waves in (low-density, primarily neutral) molecular clouds [Hennebelle, 2013, Mouschovias, 1991]. However, the subject is still under debate.

Miville-Deschenes et al. [2010] published a power spectrum analysis of Polaris Flare, from data obtained by Herschel-SPIRE of a 250  $\mu\text{m}$  map (Fig.1.3). It is well fit by a power law from 2 pc to 0.02 pc, which indicates that the cloud doesn't have a characteristic scale and is supposed to be dominated mainly by turbulence. However, the distribution of filament widths in this cloud, has a prominent peak near 0.1 pc [Arzoumanian et al., 2011, Panopoulou, Psaradaki & Tassis, 2016]. Regarding this, we would expect that, the power spectrum should reveal the imprint of the characteristic width. This inconsistency motivated us to study the origin of the apparent characteristic width of filaments.

In this work we re-examined the steps for the construction of the widths distribution, in an image that is constructed to be scale free. This thesis begins with a brief review, in chapter 2, of the spatial power spectrum of an image, it's properties and the information it can convey about the image. In chapter 3, the process for deriving the spatial power spectrum is described. We performed this process to find out which parameters, from that we used for the image's construction, reveal a power law spectrum. In chapter 4, we briefly describe the analysis we followed to construct the distribution of the widths and found to have a broad peak. In order to understand how this arised, we simulated the above analysis (chapter 5) and found that the averaging along individual filaments, has as a consequence this small spread to appear, as it is verified also by the Central Limit Theorem (CLT). In addition, the simulations revealed that the longer the filaments are the narrower the distribution is. Finally, we summarize and discuss our results in chapter 6.

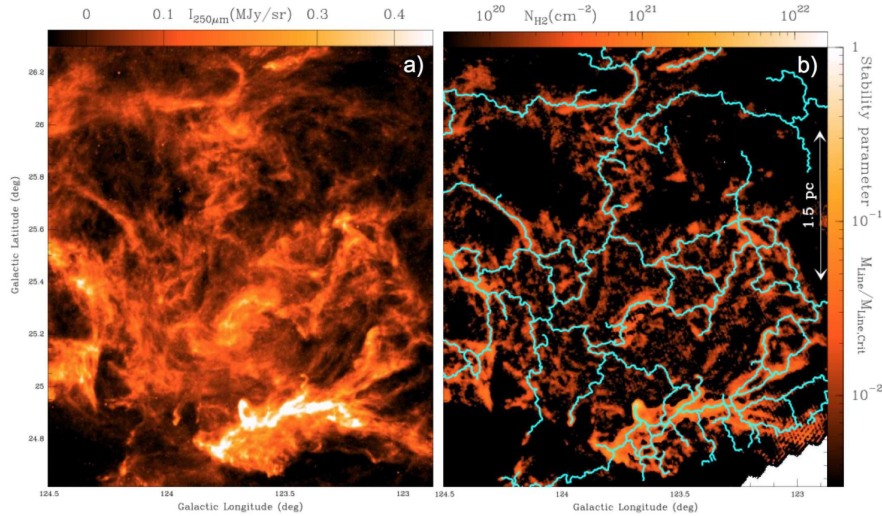


**Figure 1.1:** **Left:** *Herschel*/SPIRE 250  $\mu\text{m}$  dust continuum map of a portion of the Polaris Flare translucent cloud [Miville-Deschenes et al., 2010, Ward-Thompson et al., 2010]. **Right:** Corresponding column density map derived from *Herschel* data [André et al., 2010]. The skeleton of the filament network identified with the DisPerSE algorithm [Sousbie, 2011] is shown in light blue.

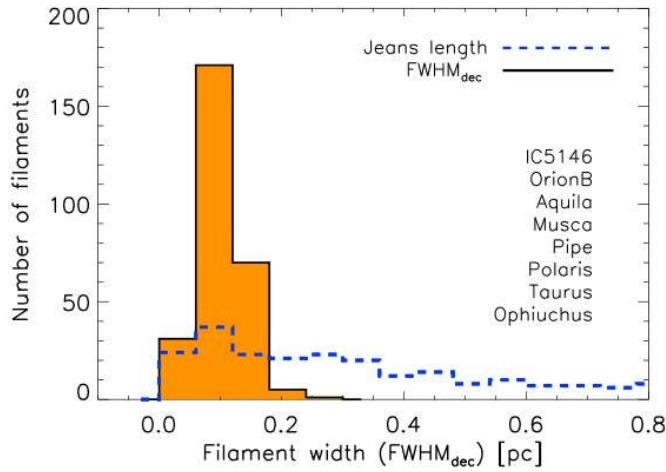


**Figure 1.2:** Histogram of deconvolved FWHM widths for a sample of 278 filaments in 8 nearby regions of the Gould Belt survey. The peak is round to 0.1 pc [Arzoumanian et al., 2011].

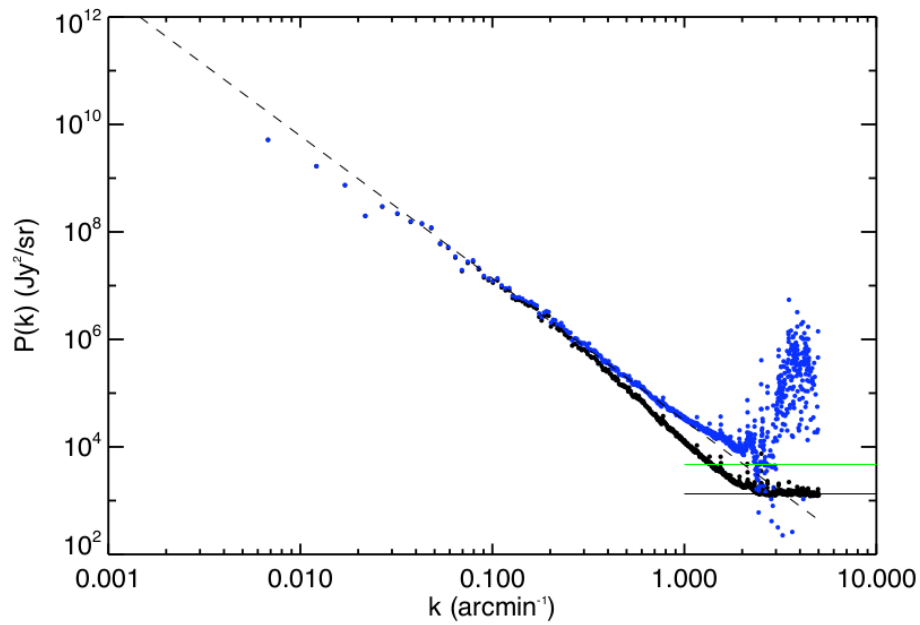


**Figure 1.3:** The black dots are the raw power spectrum (computed with an apodization of 0.97). The horizontal black line is the white noise level estimate. Blue dots are the power spectrum noise removed and divided by the psf estimated on Neptune observations. The green horizontal line and the dashed line are the source and interstellar components estimated from the blue dots power spectrum respectively, on scales  $0.025 < k < 2$  arcmin [Miville-Deschenes et al., 2010].



# Chapter 2

## Power Spectral Density

The *Power Spectral Density* (or Power Spectrum) shows, how the power of a signal is distributed over frequency. If  $H(f)$  is the Fourier Transform (FT) of the  $h(t)$  function and  $\Re$  is the real and  $\Im$  the imaginary part of  $H$ , the Power Spectrum (PS) is the squared amplitude [Press, William H. Numerical Recipes in C: The Art of Scientific Computing. Cambridge U.a.: Cambridge U Pr.]:

$$P_h(f) = |\Re|^2 + |\Im|^2$$

so that the total power is the integral of  $P_h(f)$  from 0 to  $\infty$ . The PS is the plot of power versus frequency. One can recognize from this the signal's sources. It is defined also in 2-D functions.

### 2.1 One Dimensional Power Spectrum

Consider the function  $x(t) = \sin(2\pi * 50t) + \sin(2\pi * 120t) + \text{random noise}$ . The noise is mixed with the function components in such a way that you can't recognize the signal. In order to distinguish the signal's components from the noise, you can use the power spectrum. In Fig.2.1 the PS of the  $x(t)$  is illustrated. As we can see the spectrum reveals two prominent peaks at frequencies 50 and 120 Hz, which correspond to the function's sine components.

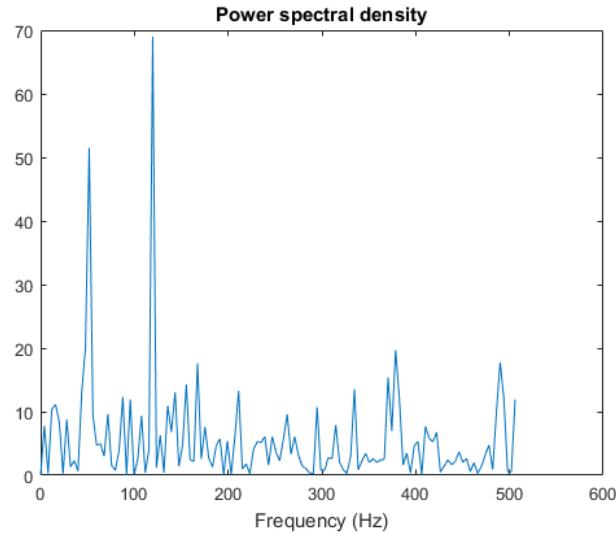


**Figure 2.1:** Power spectrum of the function  $x(t)$ . The peaks at 50 and 120 Hz correspond to the frequencies of the components of the signal.

## 2.2 Two Dimensional Power Spectrum

We are going to process digital images, so two-dimensional FT is needed for this purpose. Consider that we have a digital image with resolution  $N \times N$ . The image can be represented by a function  $h(x, y)$  and is the intensity of the pixel with coordinates  $(x, y)$ . The  $h(x, y)$  function is a 2-D array and  $x, y$  are the number of the column and row, where the pixel with intensity  $h$  is located. The *Discrete Fourier Transform* (DFT) of a 2-D function  $h(x, y)$  is  $H(u, v)$ , where  $u$  and  $v$  are the spatial frequencies of  $x$  and  $y$  respectively and is called *Spatial Power Spectrum (SPS)*. Let  $P(u, v)$  be the 2-D SPS, it is defined as the squared amplitude of  $H(u, v)$ .

### 2.2.1 Properties of 2-D Power Spectrum

The SPS has two basic properties. First of all it is *periodic*. The transformation treats an image as if it were part of a periodically replicated array of identical images extending horizontally and vertically to infinity (Fig 2.2, left panel). So does the 2-D spectrum. Hence, it repeats itself endlessly in both directions with period  $N$  (Fig 2.2, right panel). The DFT computed for a  $N \times N$  image is a single period from this infinite sequence, so  $N \times N$  coefficients

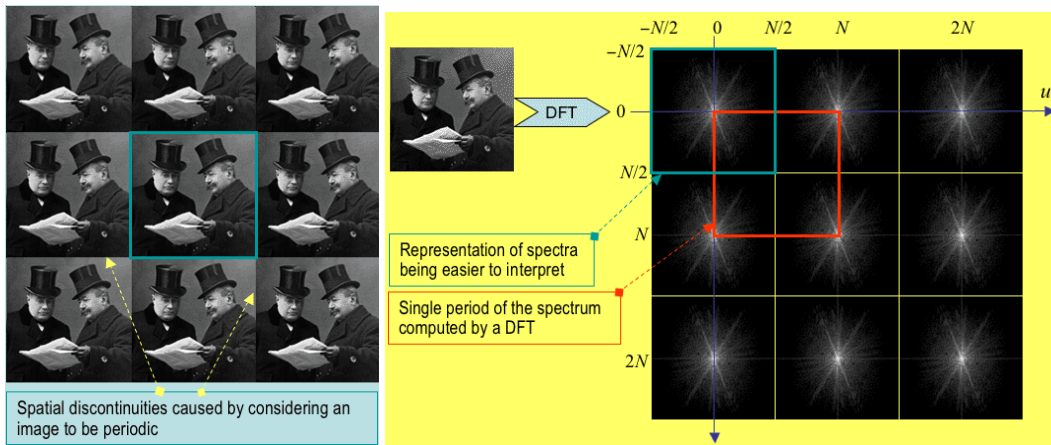


**Figure 2.2:** **Left:** FT repeats an image up and down to infinity. Between adjacent images some discontinuities are created and as a result of them, bright lines across the central axes of Power Spectrum are created. **Right:** Power Spectrum as treated by FT. In the red box is a single period spectrum computed by DFT. The blue box is the shifted representation of the same spectrum.

of the FT are calculated.

The second property comes from the fact that images are real functions. If a function is real, then  $|H(u, v)| = |H(-u, -v)|$ . This means that for positive frequencies  $u, v$ , there are negative frequencies  $-u, -v$ , corresponding to the same value of the spectrum. As a result of this, mirror images of negative frequencies, which correspond to positive frequencies spectra, are created. This property is called *complex conjugate symmetry*.

The spectrum that Fourier reveals, is a single period of the infinite spectra sequence computed from 0 to  $N$ , in both  $u$  and  $v$  directions. Due to periodicity and conjugate symmetry, the spectrum of a single period is divided in four equal quadrants, as illustrated in the red box in Fig 2.2, right panel. In Fig 2.3, (b), one can see how the frequency increases in a single period spectrum. The interpretation of the SPS is made much easier if the results of DFT are centered on the point  $(u=0, v=0)$ , such that the frequencies increase in any direction away from the center (Fig 2.3, (d)). This can be done by circular shifting of the four quadrants of the spectrum. As a result of the shift, the computing sum of DFT starts from  $-N/2$  to  $N/2$ , rather than from 0 to  $N$ .

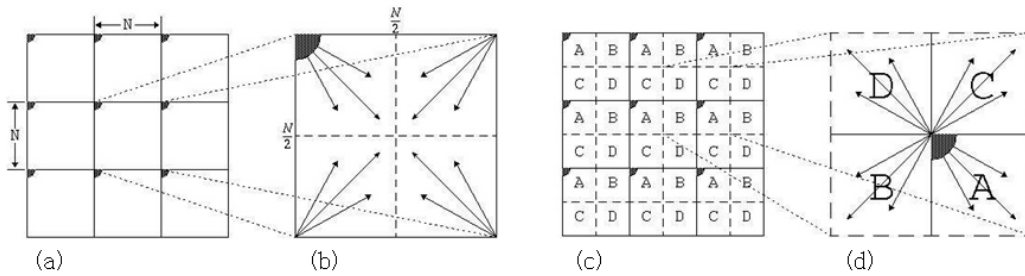


**Figure 2.3:** (a) The FT treats the image as if it is repeated endlessly in both directions, where (b) the frequency in the 2-D spectra increases along the direction of arrows (c) The quadrants of the spectrum are then shifted (d) so that the frequency increase in every direction away the center

In Fig 2.2, right panel, the blue box, shows how the primal spectrum (red box) looks like after it has been shifted . The shift is nothing more than a change in the center of the coordinate system, in the frequency domain, from  $(N/2, N/2)$  to  $(0,0)$ . The last step to derive a completed Power Spectrum is to use non-linear mapping, usually log scale. This comes from the fact that lower frequencies dominate over the mid-range and high-frequency and if we use linear scaling, the only thing that we are going to see is a bright point in the middle of the spectrum.

### 2.2.2 Examples of 2-D Power Spectra

In Fig 2.4 there are two examples of SPS. The upper images are pure sine waves, while underneath of each image its 2-D spectrum exist. In the Power Spectra the centred dot is the DC term (zero frequency term), which represents an average brightness across the image. The distances in this picture correspond to a frequency magnitude hence to a specific length scale of the real image. High frequencies correspond to low, while low frequencies to high length scales. As we can see, in the SPS image of the left horizontal sine wave, two dots are distinguished except the zero frequency dot. They are symmetrically placed and they represent the frequency of the wave. The image is represented by a real function, hence there are two frequencies, a positive and a negative, that correspond to wave's frequency magnitude. The right sine wave image, is rotated and so the FT is rotated. This spectrum has white lines across the central axes and they look like a white cross. This

phenomenon is known as *Gibbs Effect* and it takes place, due to the periodicity of FT. As we have discussed above, the transformation repeats an image endlessly in both direction. The periodicity creates these discontinuities, Fig 2.5, causing edge effects.

Before we go through our image analysis, we present a paradigm of a real image. In Fig 2.6, left panel, an image with pellets is illustrated, while the right panel is their spectrum. It is obvious that the pellet's SPS reveals a circular symmetry. Generally the spectrum follows the symmetry of the real image. This concentric ring structure is due to each individual pellet and we would still get this pattern from an image with just one pellet.

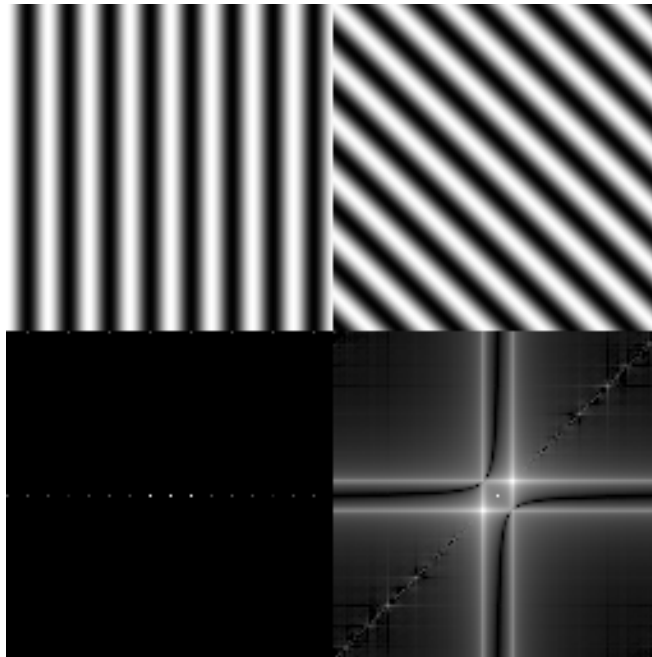


**Figure 2.4:** The underneath images are the 2-D Power Spectra of the sine waves above. In the rotated sine wave spectrum, the white cross is due to the edge effects

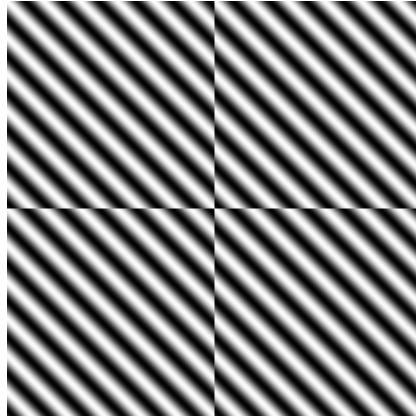


**Figure 2.5:** In this figure it is illustrated, how the FT treats an image of a rotated sine wave. Discontinuities between the repeated images appeared causing the edge effects we observe in SPS.

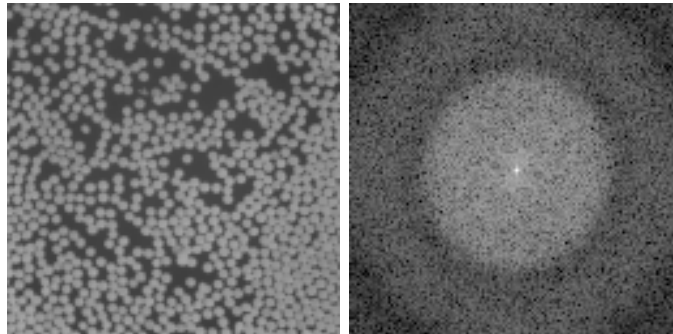


**Figure 2.6: Left:** Circular pellets **Right:** The Power Spectrum of the pellets reveals their circular symmetry.

# Chapter 3

## Azimuthally Averaged Power Spectrum

The first step of our work is to create a filamentary scale free image, in which we can apply Arzoumanian et al. [2011] methodology. To construct the image we used the Ridged Multifractal model from the suite of noise-synthesis models implemented in the python library pynoise (**Panapoulou et al. 2016**). The accepted parameters to construct the image for our model, are chosen to result in an 1-D PS, that is power law. In this chapter we present the process for deriving the SPS. Taking the radial average of the SPS we constructed the 1-D PS of the multifractal image.

### 3.1 Derivation of SPS

The methodology for deriving the SPS is based on Pingel et al. [2006]. We start with a 2-D image, "primal" image, in which the pixels' intensity fluctuations are a function  $I$ . The 2D SPS,  $P(k)$ , is defined by Stanimirovic & Lazarian [2001] as:

$$P(k) = \int \int \langle I(x)I(x') \rangle e^{-iL \cdot k} dL, L = x - x'$$

which is the Fourier Transform of the autocorrelation function of  $I$ .  $k$  is the spatial frequency in units of wavenumber,  $k \sim 1/\lambda$ , where  $\lambda$  is the length scale and  $L$  the distance between two points in the primal image we transformed, measured in units of length. First we measure the FT of the image, calculate

the square of the modulus of the transform and then shift the 2-D power image, so that the zero frequency is shifted at the image's center. As a result, we take the "transformed" image. The distances in the "transformed" image are measured in wavenumbers,  $k$ , which means that higher distances there, corresponds to smaller in the real image. We assume azimuthal symmetry and we take concentric annuli of equal width, in logarithmic intervals, centered at the center of the image and for each annulus we calculate the median value. Each median value corresponds to the average power of the specific annulus, that was calculated, hence at a specific scale distance in the "primal" image. Based on what we discussed above, the amount of power of annuli with greater radii probe the power of smaller spatial scales, while smaller annuli probe the power of larger spatial distance. The use of median value as the proper one for the power, was motivated by the fact that Pingel et al. [2006], found by simulations, that if the distribution data values is Gaussian, the average power per annulus is well represented by the median value. The edge effects, due to Gibbs Effect, introduce a high end tail in data's distribution. Finally, the median power is plotted as a function of spatial scale. The code was written in Python 3.0.

### 3.1.1 From Spatial to Frequency Domain

In the previous chapter, we have discussed that the frequency domain, for an image with  $N \times N$  resolution, ranges from  $-N/2$  to  $N/2$  for every dimension. The values of  $-N/2$  and  $N/2$  corresponds to the Nyquist frequency, which is defined as  $f_c = \frac{1}{2D}$ , where  $D$  is the spatial interval between two pixels. We can arbitrarily set  $D=1$  cm. Then the Nyquist frequency is equal to  $0.5\text{cm}^{-1}$ . Therefore  $N/2$  pixels in the frequency domain correspond to  $0.5\text{cm}^{-1}$ . The amounts are proportional, so for  $X$  pixels in frequency domain we can find it's frequency value. The inverse of the frequency is a specific scale distance in the image. Greater values of  $D$  just multiply the distant scales with a constant factor, but since we are not interested in the real distances and we measure in pixels,  $D$  can be equal to one for simplicity.



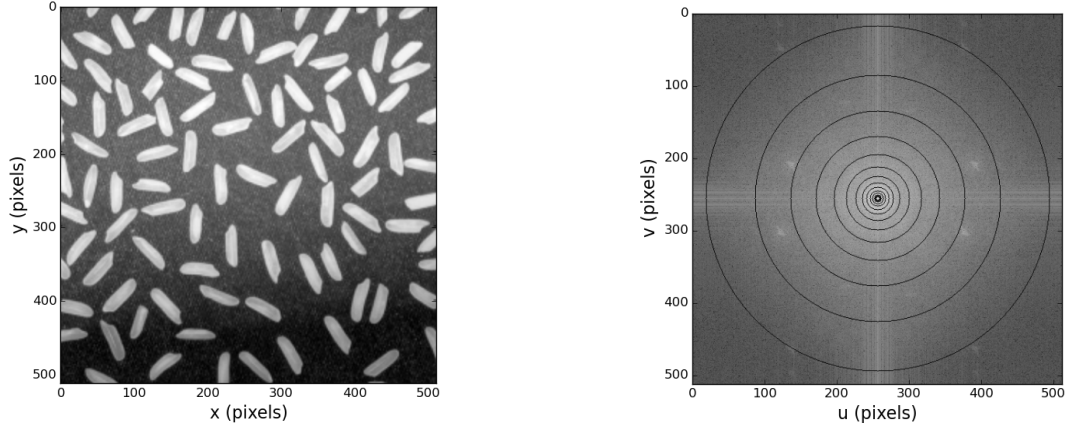


**Figure 3.1: Left:** An image with rices. The resolution is  $512 \times 512$ . **Right:** The 2-D Spectrum of the rice image. The concentric annuli are illustrated.

## 3.2 Verification of the Code

In order to be sure that our code is right, we took an image with rices of average width  $\sim 18$  pixels and average length  $\sim 55$  pixels. (Fig 3.1, left panel). The resolution of the image is  $512 \times 512$ , thus the Nyquist frequency corresponds to 256 pixels. We followed the process mentioned above by taking fourteen concentric annuli (Fig 3.1, right panel), taking into account that the distribution of data must follow a Gaussian (Fig 3.2), and then we derived the PS of the image, Fig 3.3. The upper horizontal axis corresponds to distances in the image, while the lower axis corresponds to the values of frequencies. In the figure, two vertical lines are illustrated. Each line corresponds to the value of the mean width (dotted) and length (solid) of the rice, respectively. At these values in the diagram some rapid changes occurred indicating the existence of these characteristic distant scales. Therefore, our algorithm verified the expected values, hence is appropriate for use.

## 3.3 SPS of Fractal Image

The image we constructed for the analysis is illustrated in Fig 3.4. As we can see, it appears filamentary. Following the procedure, described above, we obtain the SPS. We took ten concentric annuli, Fig 3.5, and then we derived

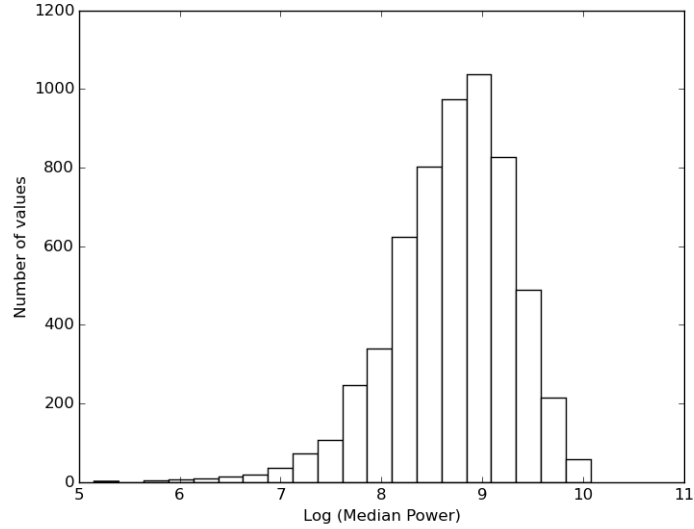


**Figure 3.2:** The distribution of data of the 2-D rice spectrum for 88 pixels radius. The shape follows a Gaussian with a high end tail, caused by the edge effects.

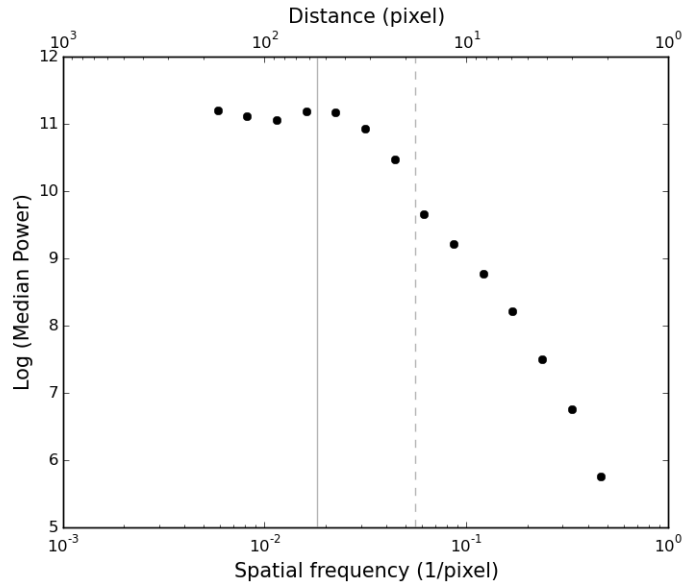


**Figure 3.3:** The PS of the rice image. The dotted and the solid vertical lines, are for the width and the length values of the rices respectively.

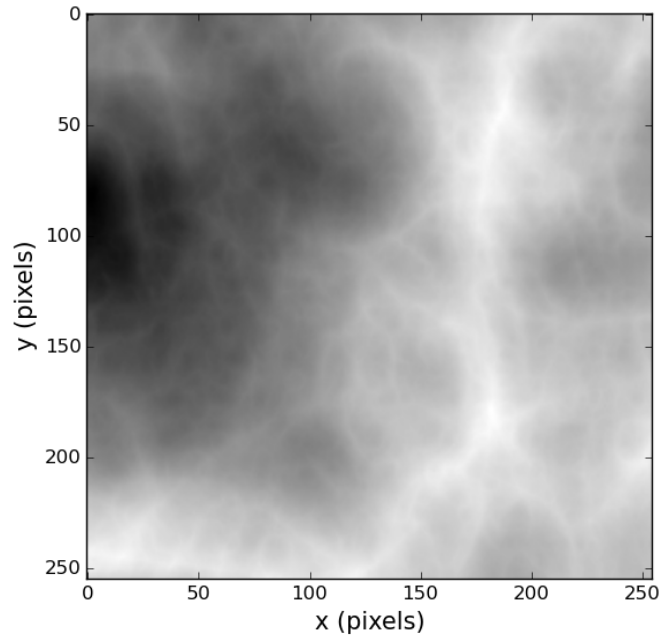


**Figure 3.4:** The multi-fractal image we constructed for our analysis.

the PS (Fig 3.6) which has the form of a power law.

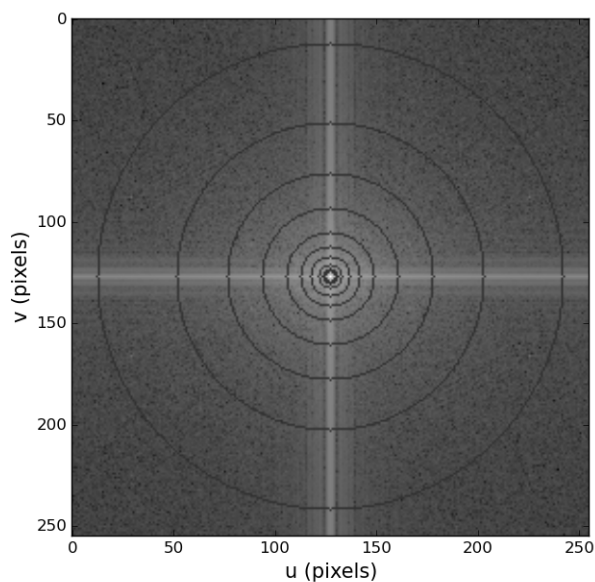


**Figure 3.5:** The SPS of the fractal image.

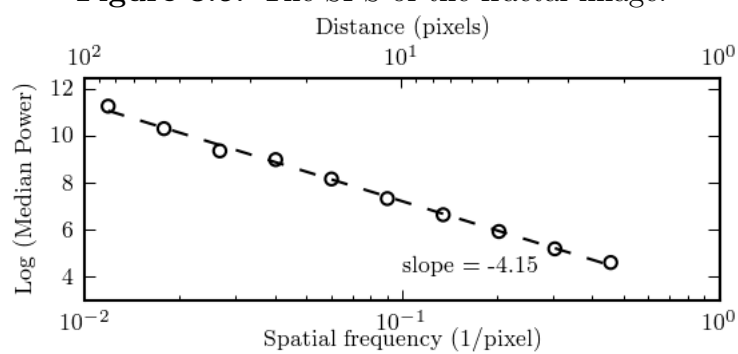


**Figure 3.6:** Fractal's Power Spectrum and linear fit in log space.

# Chapter 4

## Filament Identification and Analysis of Fractal Image

In this chapter, we present our results, when we applied an analysis similar to Arzoumanian et al. [2011] to the fractal image.

### 4.1 The Methodology

We employ Discrete Persistent Structures Extractor DiSperSe algorithm (DiSperSe, Sousbie [2011]), which traces the filaments and produces the skeleton of the image. DISPERSE analyses the topology of a given map and extracts its skeleton, which corresponds to the ridges of elongated structures. Next, we provide the skeleton of DiSperSE and its corresponding image as input to the Filament Trait-Evaluated Reconstruction (FILTER) code [Panopoulou et al., 2014]. The objective of FILTER is to re-process the skeleton of DiSperSe to only include continuous, non-spurious, structures and measures the width of each intensity profile along a filament. It re-process the skeleton by rejecting intensity profiles of each cross-section, along the filament structures that are not peaked around the filament ridge and above the noise-level. The filament widths are measured by fitting Gaussians iteratively to smaller and smaller distances from the filament ridge. The width is defined as the FWHM of a Gaussian with offset fit to the inner-most part of the profile [Arzoumanian et al., 2011]. Finally, only sufficiently elongated structures (with at least a 3:1 length to width ratio) are included in the final sample of filaments that we consider for further analysis.

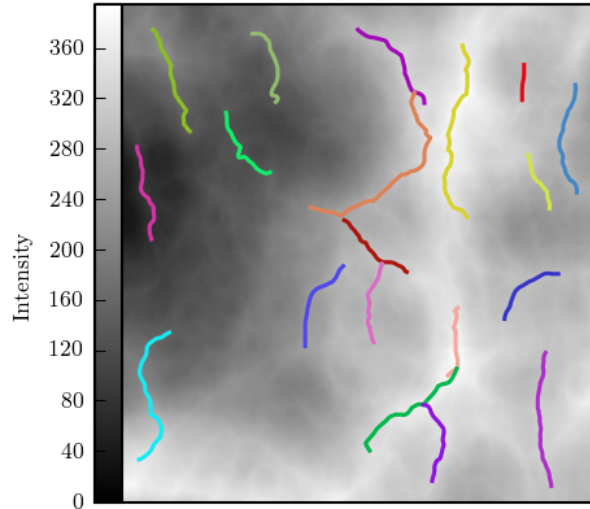


**Figure 4.1:** Image generated using Ridged Multifractal Noise, with the skeleton of filaments having an aspect ratio of at least 3:1 overplotted.

## 4.2 Analysis Results

We performed the methodology described above, in the multi-fractal image. The filamentary network produced by DiSperSE and FILTER is illustrated in Fig 4.1. We constructed the distribution of the average width values of the identified filaments. The distribution is illustrated in Fig 4.2 and follows the Gaussian shape, peaked at around 12 pixels. Its deviation is 3.8 pixels (**G.V.Panopoulou et. al 2016**). Therefore, we have a situation similar to that of Polaris, where in a scale free image the distribution of widths reveals a prominent peak. This implies that the "characteristic width" is probably related to the selected methodology for analysis.

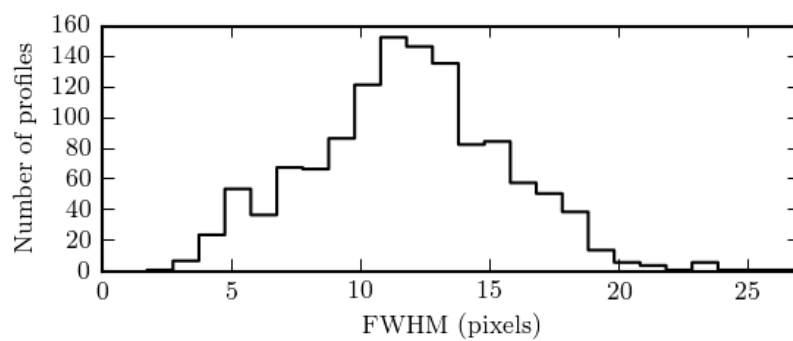


**Figure 4.2:** The distribution of the mean value of the widths of the filaments tha DiSperSe and FiLTER identified in the fractal image. The peak is at 12 pixel and a standard deviation of 3.8.

# Chapter 5

## Simulations

The distribution of the widths in the Polaris Flare has a spread of 0.05 pc and is peaked near the sensitivity limit. The combined distribution of the averaged widths from filaments of different clouds is a well peaked Gaussian with a spread of 0.03 pc [Arzoumanian et al., 2011]. This small spread is implied as the "characteristic width". We attempt to understand why after averaging, the distribution is modified to Gaussian, the reason the spread is narrower than the pattern distribution and what parameters affect. In addition, we compare it with a non-averaged distribution, which include measured widths independent of the filament they belong (e.g Panopoulou, Psaradaki & Tassis [2016]).

For the clouds Polaris, Aquila and IC5146 we constructed the normalized distribution of the averaged and non-averaged widths (Fig 5.1), following the methodology described in the previous chapter. The solid line is the distribution of all FWHM, while the dotted line is the distribution of the averaged FWHM. As we can see the shape of the distributions is clearly different. The non-averaged have long tails at scales larger than 0.15 pc and fall rapidly near the sensitivity limit. The averaged are Gaussians peaked at the mean value of the pattern distributions. The bottom panel in this figure shows the distribution of the three clouds together.

The Gaussian shape of the averaged, can be explained from the Central Limit Theorem (CLT). According to this, the average values of samples with well defined expected value and finite variance, will be normally distributed, regardless of the pattern distributions. In our situation, the averaged FWHM are approximately 0.1 pc, following the pattern distribution illustrated in Fig 5.2, hence their distribution is a Gaussian peaked at this value. However, the



widths aren't totally independent so the expected spread of the Gaussian is different than that expected from CLT.

## 5.1 The Methodology

We simulated the two methods of widths distribution construction, using random numbers, in order to find out which parameters affect more the analysis. We created a code that takes two distribution as input. The first input is the distribution of filaments widths (Fig 5.2), while the second is the distribution of the filaments sizes (Fig 5.3) (number of profiles contained per filament). It calculates the CDF of the given distributions and calculates the analytical form of the functions. By using these functions, it creates  $N$  groups of random numbers, which follow the input width distribution and each group has total size considered by the size distribution. Then it constructs the averaged and non-averaged distributions, as shown above. The code was written in Python 3.0.

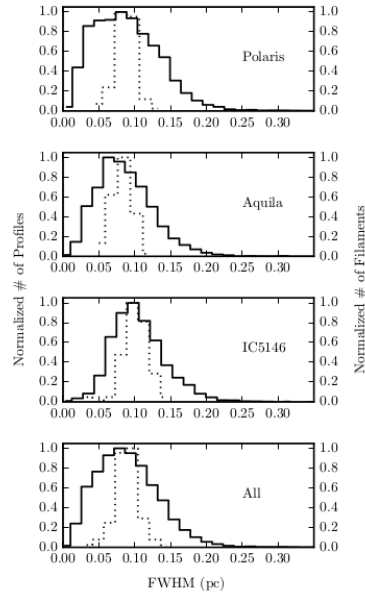


**Figure 5.1:** Normalized distributions of the averaged (dotted) and the non-averaged (solid) widths for the clouds Polaris, Aquila, IC5146.

### 5.1.1 Verification of the Code

First of all, we want to verify that our algorithm was programmed right. In order to do it, we set the group's sizes to have the same value and we were increasing the number of  $N$  groups and decreasing their size and then getting their non-averaged distributions. The distributions we take as output must have shapes that are similar to the pattern.

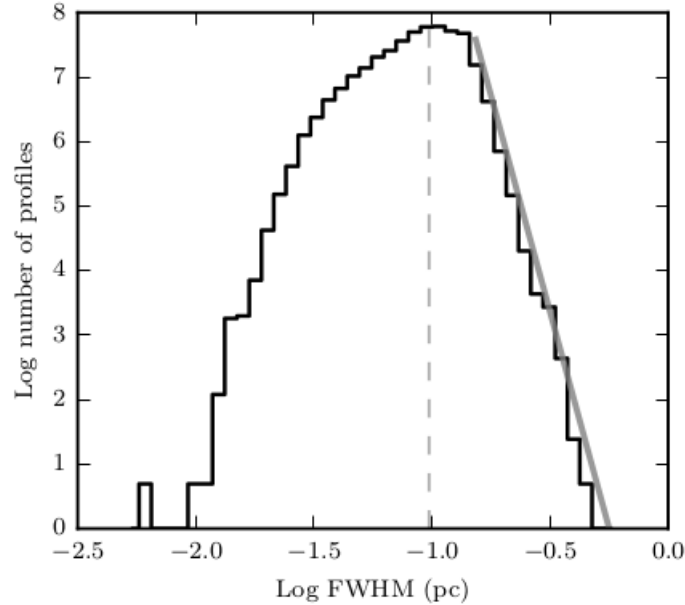
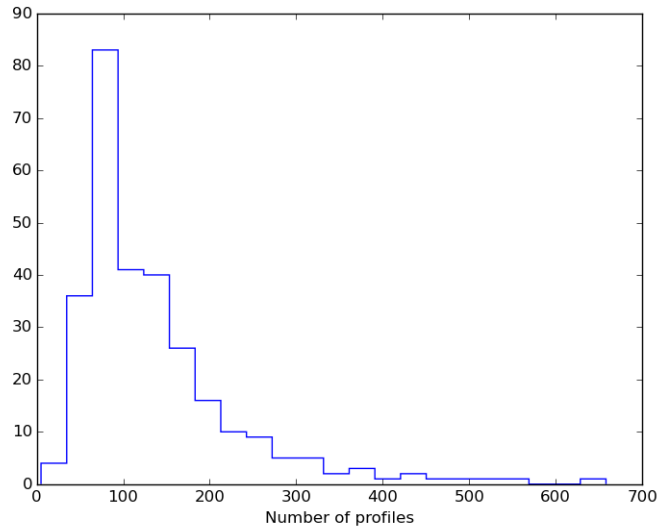


**Figure 5.2:** Distribution of all profile widths of filaments in the Polaris Flare. At scales larger than 0.15 pc, the distribution resembles a power law (gray solid line is a linear fit to the logarithmically-spaced bins). The mean of the distribution is shown by the gray dashed vertical line.

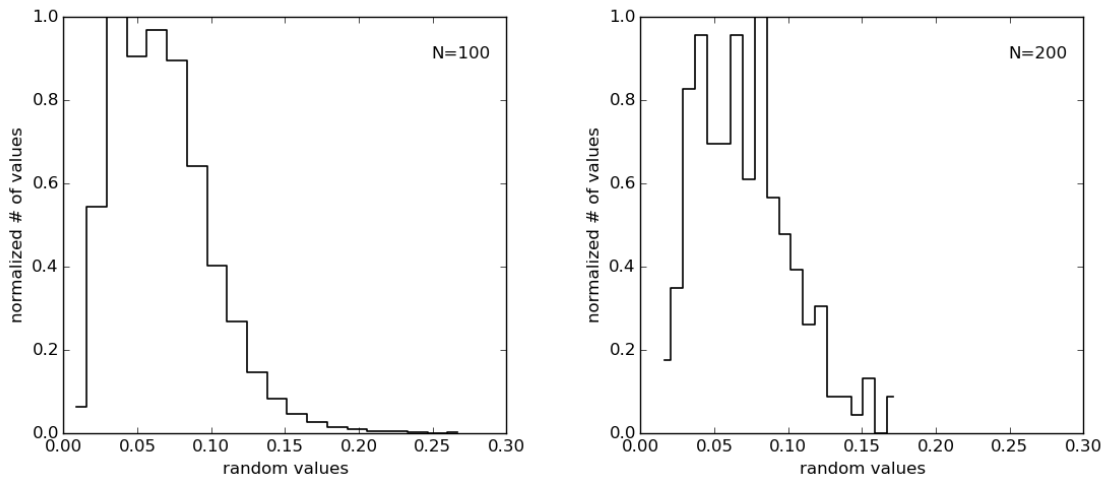
We started with  $N=100$  groups, each of them consist of 100 random number. The increasing and decreasing step is equal to 10. So the first simulation is for  $N=100$  groups, consisting of 100 numbers. The second is for 110 groups with 90 numbers etc. The last one is for 200 groups with only 1 number. In Fig 5.4 are illustrated the normalized distributions of the 100 and 200 groups respectively, as indicative figures. As you can see from the distributions, even in the limit case of 200 groups which contain a unique value, their shapes are similar to the pattern. Hence, we are sure that the algorithm is appropriate for our analysis.

## 5.2 Analysis

We performed simulations for different values of  $N$ . The result of the simulations revealed that the averaged values are concentrated near the mean value of the non-averaged. In Fig 5.6, are illustrated the averaged (dotted)



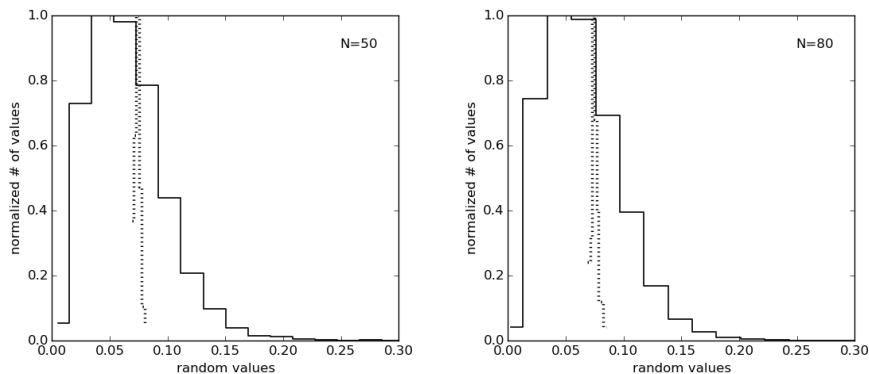
**Figure 5.3:** The distribution of filaments size of Polaris Flare. The size of a filament is the number of profiles that contains. As is illustrated most of the Polaris filaments contain round 90 profiles.



**Figure 5.4:** Normalized distribution of  $N=100$  groups (left panel) and of  $N=200$  groups (right panel).

and the non-averaged values (solid) distributions. From the figures we can see that, is verified the statement of CLT that, the averaged follow a Gaussian independent of the pattern distributions and that increasing the  $N$ , the shape of the averaged is getting closer to Gaussian. In table 5.1, there are the mean values and the standard deviations of the distributions. It is clear that the mean values of the two distributions are similar, while the deviations of the averaged value distributions, is one order of magnitude lower than the non-averaged. In addition the averaged deviations remain approximately constant as the  $N$  increases.

The next parameter to check, is the number of profiles in filaments. The profiles are equal to the length of a filament, because the longer a filament is, the more profiles it contains. For example, if one traces the filamentary network of a cloud with two different algorithms, which one of them traces longer filaments than the other, how is the averaged distribution affected? For that reason we performed simulations, at which we set the size of the groups to be the same and we were increasing it, for given  $N$ . The distributions are similar to that of Fig 5.6. We present only the numerical results for  $N=278$  in table 5.2. The results are similar for other values of  $N$ , too. As we increase the size of the groups, the deviation of the averaged decreases. This is reasonable taking into account the CLT. According to this, the deviation of the averaged distribution is inverse proportional of the square root of the number of samples. In Fig 5.8 are illustrated the simulations for  $N=10$ . It is obvious that the increase in the size of groups, can't reproduce the shape of the Gaussian averaged distribution.



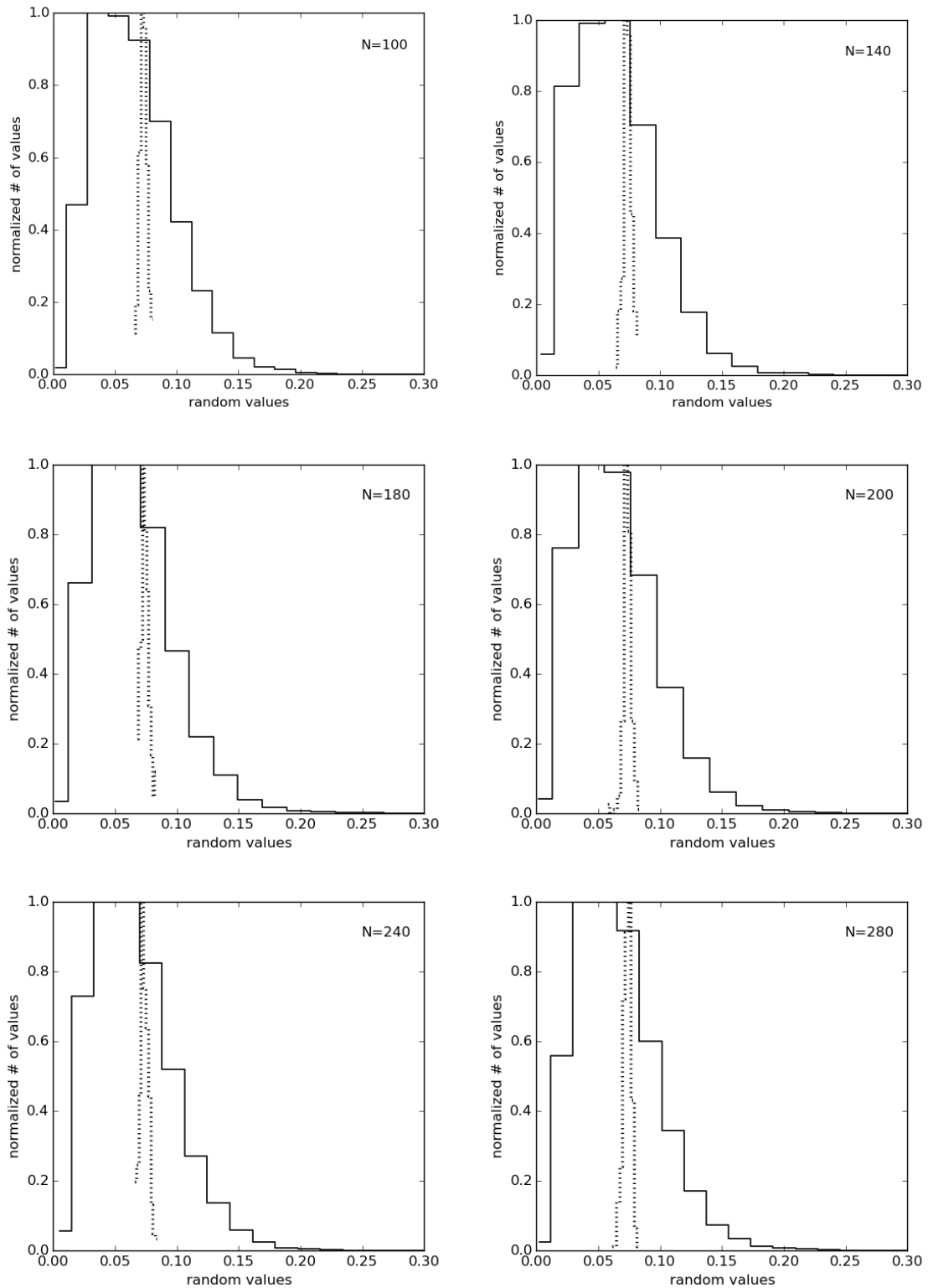


**Figure 5.6:** The distributions of the averaged (dotted) and non-averaged (solid) values for different  $N$  values.

**Table 5.1:** Mean values and standard deviations of the distributions that are illustrated in Fig[].

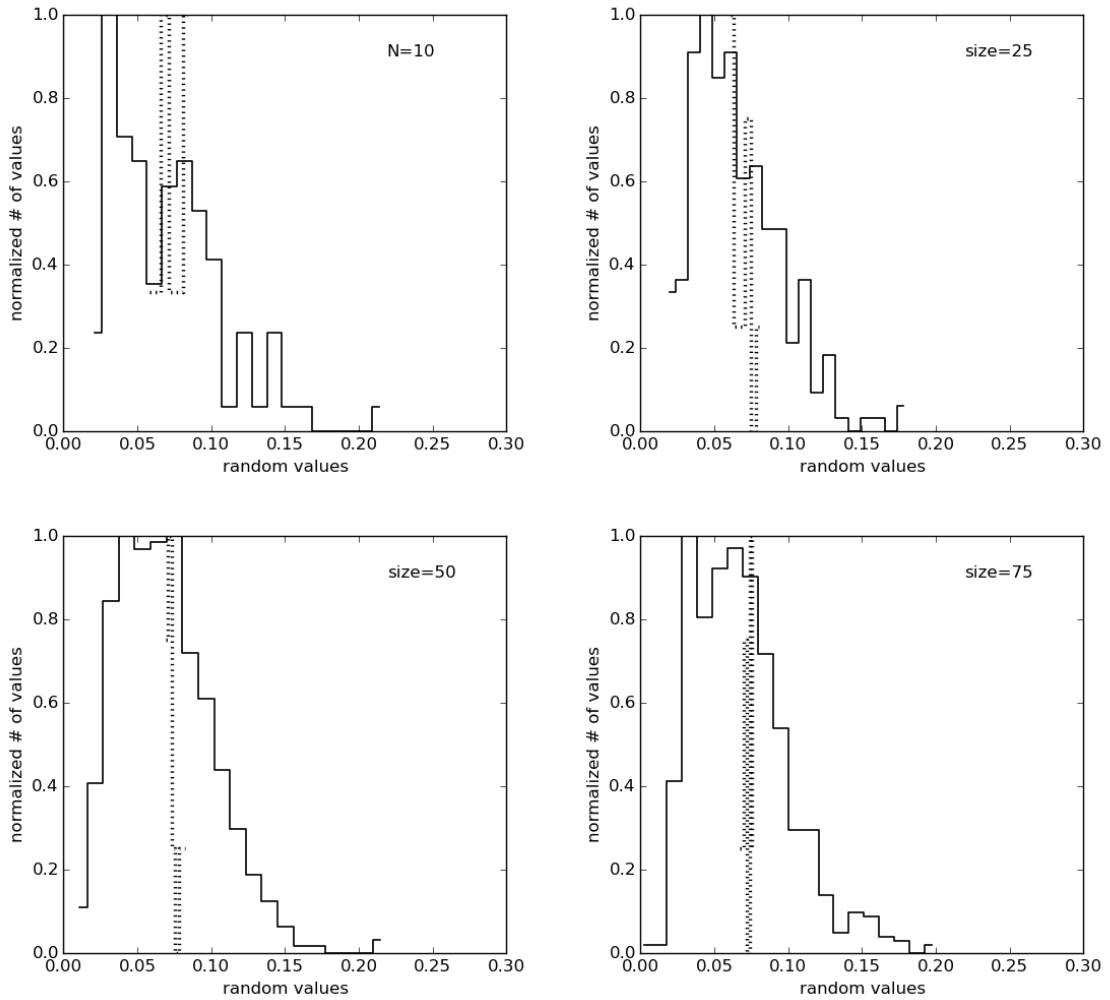
Number of Groups	STD (averaged)	Mean (averaged)	STD (non-averaged)	Mean (non-averaged)
50	0.0035	0.0940	0.0323	0.0943
80	0.0027	0.0945	0.0331	0.0945
100	0.0034	0.0949	0.0330	0.0947
140	0.0034	0.0944	0.0330	0.0945
180	0.0036	0.0943	0.0330	0.0942
200	0.0030	0.0940	0.0323	0.0941
240	0.0035	0.0945	0.0332	0.0945
280	0.0035	0.0944	0.0328	0.0945

**Table 5.2:** Mean values and standard deviations of the distributions for N=278.

Size of Groups	STD (averaged)	Mean (averaged)	STD (non-averaged)	Mean (non-averaged)
10	0.0109	0.0951	0.0327	0.0951
25	0.0070	0.0951	0.0335	0.0952
50	0.0045	0.0942	0.0332	0.0942
75	0.0038	0.0948	0.0328	0.0948
100	0.0035	0.0946	0.0328	0.0946
150	0.0028	0.0948	0.0328	0.0948
200	0.0024	0.0945	0.0329	0.0945
250	0.0021	0.0945	0.0331	0.0945
278	0.0019	0.0946	0.0329	0.0946

### 5.3 Analysis Results

To sum up, the simulations revealed that the averaged distribution is a well defined Gaussian, regardless of the pattern distribution. As more filaments are examined the averaged distribution is getting closer to Gaussian's shape, while it's deviation remains almost constant. The number of profiles per filament affects only the deviation of the averaged distribution. If the size of filaments is increased, the deviation is decreased, thus the Gaussian is narrower for longer filaments, as it is verified by the CLT.



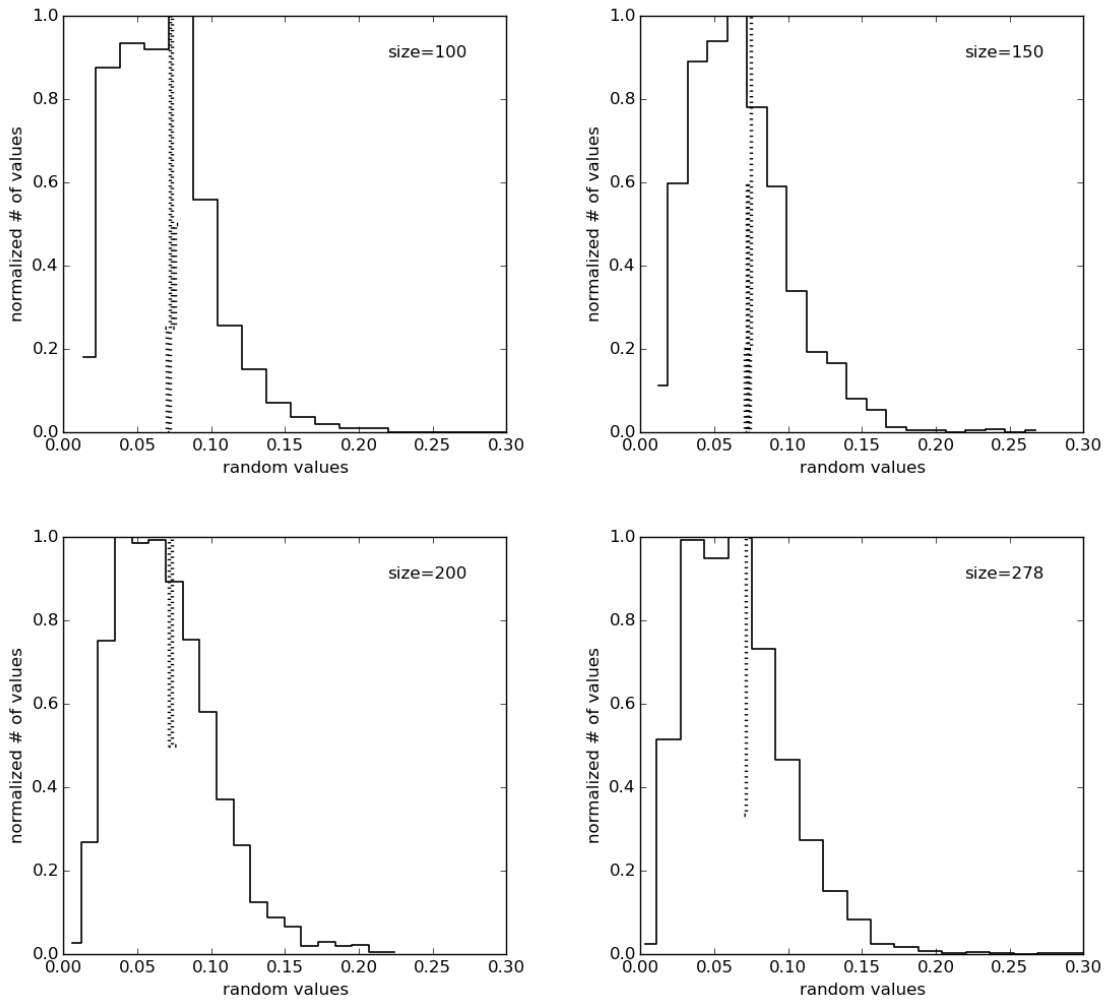


**Figure 5.8:** The distributions for  $N=10$  of the averaged (dotted) and non-averaged (solid) values for variable group's size.



# Chapter 6

## Conclusion

In this work we have examined the analysis of filament widths in order to find out, how the "characteristic width" appears in Polaris Flare power spectrum, which has the form of a power law.

From our analysis, we can conclude that the methodology of Arzoumanian et al. [2011], for measuring widths, creates a peaked distribution in an image without preferred scale. Since a similar situation arise in Polaris Flare, it is doubtful whether the "characteristic width" appeared as a consequence of gravity instability and it is not a matter of the selected methodology. The simulations revealed that the process of averaging over filament profiles, results in a distribution that has the form of a Gaussian, as a result of the CLT. The more filaments examined the distribution gets closer to Gaussian shape, while its spread is determined by the number of filament profiles. The distribution becomes narrower as more filament profiles are averaged.

The present study could be extended to include as many molecular clouds as possible and compare with our results. It would be of great interest to find out the reason the averaged distributions of widths of the clouds, appear the peak approximately to 0.1 pc and not to an other value.

# Bibliography

- André P. et al., 2010, A&A, 518, L102
- André P., Di Francesco J., Ward-Thompson D., Inutsuka S.-I., Pudritz R. E., Pineda J. E, 2014, Protostars and Planets VI, 27
- Arzoumanian D. et al., 2011, A&A, 529, L6A
- Miville-Deschênes M.-A. et al., 2010, A&A, 518, L104
- Molinari S. et al., 2010, A&A, 518, L100
- Hennebelle P., 2013, A&A, 556, A153
- Könyves V. et al., 2015, A&A, 584, 91
- Mouschovias T.C., 1991, NATO ASIC Proc. 342: The Physics of Star Formation and Early Stellar Evolution, 449
- W.H.Press, S.A. Teukolsky, W.T. Vetterling, B.P. Flannery, 1992, *Numerical Recipes in C: The Art of Scientific Computing*, Second Edition, CAMBRIDGE UNIVERSITY PRESS
- Padoan P., Goodman A. A., Draine B. T., Juvela M., Nordland . R, Rögnvaldsson O. E., 2001, ApJ, 559, 1005
- Panopoulou G. V., Tassis K., Goldsmith P. F., Heyer M., 2014, MNRAS, 444, 2507P
- Panopoulou G. V., Psaradaki I., Tassis K., 2016, MNRAS, 462, 1517P
- Pingel N. M. et al., 2006, ApJ, 779, 36
- Porter D. et al., 1994, Phys. Fluids, 6, 2133

Sousbie T., 2011, MNRAS, 414, 350

Stanimirović S. & Lazarian A., 2001, ApJ, 551, L53

Vázquez-Semadeni E., 1994, ApJ, 423, 681

Ward-Thompson D. et al., 2010, A&A, 518, L92